A Superelastic Shape-Memory-Alloy Beam Model

Ferdinando AURICCHIO[o] & Elio SACCO[+]

[o] Dipartimento di Ingegneria Civile, Università di Roma "Tor Vergata" (Italy)

[+] Dipartimento di Ingegneria Industriale, Università di Cassino (Italy)

Abstract

The present paper proposes a simple *shape-memory-alloy* beam model, based on the classical Euler-Bernoulli beam theory.

Due to restrictive kinematical assumptions, a one-dimensional constitutive equation is used. Thus, the material behavior is described through a simple 1D phenomenological model, which allows for different material responses in tension and compression as well as for different elastic properties between austenite and martensite.

Two numerical procedures are developed for the determination of the cross-section response together with a time-step integration algorithm. Then, the implementation of the shape-memory-alloy beam model within a finite-element framework is addressed.

Several numerical examples are investigated to assess both the performance of the beam model and the procedure developed. The complex behavior of a typical cross-section is emphasized. The results obtained from the simulation of three- and four-point bending tests are compared both with experimental results and with numerical solutions obtained from a three-dimensional finite-element scheme.

1 Introduction

Shape-memory alloys (SMA) are materials able to change their crystallographic structure depending on the temperature and the state of stress [1, 2, 3].

These changes are, in general, interpreted as martensitic transformations, that is, solid-solid, diffusionless transformations between a crystallographically more-ordered parent phase (*austenite*) and a crystallographically less-ordered product phase (*martensite*) [4, 5]. The activation and the evolution of these phase transformations depend on stress and temperature. Moreover, for shape-memory alloys the transformation is reversible and, in many cases, rate-independent [6].

As a natural consequence of the microscopic properties, shape-memory solids show unusual macroscopic behaviors. In particular, at sufficiently high temperature they present the superelastic effect, that is, the ability to recover large

deformations in loading-unloading cycles. In fact, consider a specimen in the austenitic state and at a temperature such that at zero stress only the austenite is stable; if the specimen is loaded, while keeping the temperature constant, the material presents a nonlinear behavior, due to a stress-induced conversion of austenite into martensite. Upon unloading, while again keeping the temperature constant, a reverse transformation from martensite to austenite occurs. At the end of the loading-unloading process no permanent strains are present and the stress-strain path is a closed hysteresis loop.

The superelastic effect is, in general, not present in traditional materials. Hence, shape-memory alloys lend themselves to be successfully adopted in a broad set of advanced applications [7, 8], ranging from orthodontic wires [9] to self-expanding micro-structures used in the treatment of hollow-organ or duct-system occlusions [10].

A review of the available literature and direct contacts in the industry, however, show on one hand a large interest on specific micro- and macro- constitutive aspects of shape-memory alloys, on the other hand a lack of computational tools to support the design process of SMA devices, with the exception of few examples [11, 12].

A major reason for this lack of design tools is that the development of an effective SMA constitutive model together with a robust integration algorithm is not an easy task. This is mainly the consequence that the description of phase transformations may require non-conventional theoretical frameworks, as for example done in Reference [13]. Moreover, experimental evidence shows a dependency of the material response on the deformation mode (tension, compression or shear) [14, 15].

The combination of all these aspects results in a non-trivial structural response even for very simple cases. Since in most applications the SMA structural elements are one-dimensional (1D), such as rods and beams, the development of a SMA beam model appears to be of great interest.

A first study of SMA superelastic beam elements can be found in the work of Atanackovic and Achenbach [16], who derived an explicit analytical moment-curvature relation based on a simple 1D superelastic constitutive law. A more complex stress-strain relationship has been considered by Gillet et al. [17, 18] for the analysis of SMA beams and helical springs. In particular, they used a three-dimensional constitutive law, taking into account the different material behavior in tension and in compression. Finally, Auricchio et at. simulated the response of simply supported SMA beams, through a three-dimensional superelastic finite-element model [19, 20].

The present work is devoted to the derivation of a superelastic beam model, based on the classical Euler-Bernoulli theory. The goal is to develop a simple and effective computational tool for the investigation and the analysis of a specific but frequently adopted structural typology. In fact, on one hand the beam model is simple enough to allow the use of a reduced but significant set of kinematic pa-

rameters. On the other hand, it allows one to take into account the sophisticated and peculiar material behavior.

In particular, due to restrictive kinematical assumptions, only the use of one-dimensional constitutive equations between the normal stress (σ) and the strain (ε) is required. Accordingly, in the present work the 1D material behavior is described through a simple and well-tested phenomenological model, which allows different responses in tension and compression as well as different elastic properties between austenite and martensite [21]. This model is preferred between the several ones available in literature (see for example References [21] for a partial list) since it is simple, effective and suitable of a robust algorithmic solution.

The paper is organized as follows. Initially, in Section 2 a simple SMA beam model is presented. The kinematics, the one-dimensional constitutive law and the equilibrium equations are given. Then, in Section 3 the constitutive relationships between the kinematical parameters and the beam stress resultants are derived. This nonlinear system of relations can be solved in closed form only under simplifying assumptions. In general, numerical procedures should be adopted. In particular, two iterative schemes of the Newton type are discussed in details. Section 4 is devoted to the development of a beam finite-element. Finally, in Section 5 the attention is focused on two Ni-Ti shape-memory-alloy wires for which experimental data are available. The complex behavior of a typical cross-section is studied. For three- and four-point bending tests the numerical results obtained from the proposed numerical procedures are compared with experimental data and with the solutions obtained from a three-dimensional finite-element scheme.

2 The beam model

A model for a superelastic beam subjected to both axial strain and bending is now developed. The model is based on the classical small-deformation Euler-Bernoulli beam theory [22] and, as usual, the basic ingredients are the kinematics, the local stress-strain constitutive equation and the equilibrium equations.

The beam occupies a volume V, has cross-section A and length L. Let (x, y, ζ) be a Cartesian coordinate system such that ζ lies on the center-line axis of the undeformed beam.

2.1 Kinematics

Following the Euler-Bernoulli beam theory, the cross-sections are assumed to remain plane and orthogonal to the center-line of the deformed beam. Let $\mathbf{x} = [x, y]$ denote the position vector of a typical point in the cross-section, $\mathbf{p} = [-y, x]$ the vector orthogonal to $\mathbf{x}$, and $\mathbf{s} = [u, v]$ the deflection of the beam center-line. The kinematics and the deformation of the beam are defined as:

$$\begin{array}{lcll} u_1 & = & u(\zeta) & \textit{transverse displacement} \\ u_2 & = & v(\zeta) & \textit{transverse displacement} \\ u_3 & = & w(\zeta) - \mathbf{p} \bullet \mathbf{s}'(\zeta) & \textit{axial displacement} \\ & & & \\ \varepsilon & = & \varepsilon_o - \mathbf{p} \bullet \boldsymbol{\chi} & \textit{strain} \end{array} \tag{1}$$

where $\varepsilon_o = w'$ and $\boldsymbol{\chi} = [-v'', u'']$ are the axial strain and the curvature vector, respectively, and a superscript $'$ indicates a derivative with respect to ζ.

2.2 Stress-strain constitutive equations

As briefly discussed in the Introduction, shape-memory alloys present an unusual macroscopic effect. In fact, during the loading the material can undergo large deformations, which are completely recovered during the unloading. In particular, for uniaxial states of stresses this effect is present for both tensile and compressive loading-unloading cycles (Figure 1). It is important to observe that experimental evidence has highlighted:

- a difference between the material response in tension and compression;
- a difference between the austenite and the martensite elastic properties.

The 1D constitutive relation adopted in the present work is able to reproduce the superelastic behavior taking into account both differences. Following Reference [21], let E^A and E^S be the austenite and the martensite elastic moduli, respectively, and let ξ be the martensite fraction. Then, the modulus E of the composite material (austenite-martensite) can be expressed as:

$$E(\xi) = \frac{E^A E^S}{E^S + \xi(E^A - E^S)} \tag{2}$$

The elastic constitutive relationships is set equal to:

$$\sigma = E(\varepsilon - \xi \varepsilon_L^{(\pm)}) \tag{3}$$

where ε_L is the maximum residual strain, regarded herein as a material constant [5]. The superscript $^{(\pm)}$ on ε_L indicates that the material constant may assume different values in tension and compression, indicated in the following as $\varepsilon_L^{(+)}$ and $\varepsilon_L^{(-)}$, respectively. According to this notation, the superscript $^{(+)}$ indicates a quantity relative to a tensile state ($\sigma > 0$) and the superscript $^{(-)}$ indicates a quantity relative to a compressive state ($\sigma < 0$).

The evolution of the martensite fraction ξ depends on the stress state and it is governed by the equations:

$$\begin{aligned}
\dot{\xi} &= -(1-\xi)\frac{\dot{\overline{|\sigma|}}}{|\sigma| - \sigma_f^{AS(+)}} \quad \text{for} \quad \sigma_s^{AS(+)} \leq |\sigma| \leq \sigma_f^{AS(+)} \ , \ \dot{\overline{|\sigma|}} > 0 \qquad (4)\\
\dot{\xi} &= -(1-\xi)\frac{\dot{\overline{|\sigma|}}}{|\sigma| - \sigma_f^{AS(-)}} \quad \text{for} \quad \sigma_s^{AS(-)} \leq |\sigma| \leq \sigma_f^{AS(-)} \ , \ \dot{\overline{|\sigma|}} > 0
\end{aligned}$$

for the conversion of austenite into martensite and by the equations:

$$\begin{aligned}
\dot{\xi} &= \xi\frac{\dot{\overline{|\sigma|}}}{|\sigma| - \sigma_f^{SA(+)}} \quad \text{for} \quad \sigma_s^{SA(+)} \leq |\sigma| \leq \sigma_f^{SA(+)} \ , \ \dot{\overline{|\sigma|}} < 0 \qquad (5)\\
\dot{\xi} &= \xi\frac{\dot{\overline{|\sigma|}}}{|\sigma| - \sigma_f^{SA(-)}} \quad \text{for} \quad \sigma_s^{SA(-)} \leq |\sigma| \leq \sigma_f^{SA(-)} \ , \ \dot{\overline{|\sigma|}} < 0
\end{aligned}$$

for the conversion of martensite into austenite, where $|\bullet|$ is the absolute value and a superposed bar with a dot indicates a time derivative of the overlined quantities. The material parameters $\sigma_s^{AS(+)}$, $\sigma_f^{AS(+)}$, $\sigma_s^{SA(+)}$, $\sigma_f^{SA(+)}$, $\sigma_s^{AS(-)}$, $\sigma_f^{AS(-)}$, $\sigma_s^{SA(-)}$ and $\sigma_f^{SA(-)}$represent the initial and final stress values for the transformation of austenite into martensite and for the transformation of martensite into austenite, respectively for the case of tension and compression (see Figure 1).

2.3 Equilibrium equations

The equilibrium equations can be derived by introducing the beam kinematical assumptions into the principle of virtual displacement $L_{ve} = L_{vi}$, where L_{ve} and L_{vi} are the external and the internal virtual works, respectively.

In particular, using equation (1) the internal virtual work is:

$$\begin{aligned} L_{vi} &= \int_V \sigma \ \delta\varepsilon \ dV = \int_L \int_A [\sigma \ \delta(\varepsilon_o - \mathbf{p} \bullet \boldsymbol{\chi})] \, d\zeta dA \\ &= \int_L [N\delta\varepsilon_o + \mathbf{M} \bullet \delta\boldsymbol{\chi}] \ d\zeta dA \end{aligned} \tag{6}$$

where the axial force N and the bending moment vector $\mathbf{M}$ are defined as:

$$N = \int_A \sigma \ dA \qquad , \qquad \mathbf{M} = -\int_A \mathbf{p}\sigma \ dA \tag{7}$$

The principle of virtual work returns the usual Euler-Bernoulli beam equilibrium equations, while positions (7) represent the cross-section equilibrium conditions.

3 Resultant constitutive equations

The kinematic relation (1), the local constitutive equations (2)-(5) and the cross-section equilibrium equations (7) can also be interpreted as resultant constitutive equations for the beam cross-section. In fact, they relate the stress resultants $(N, \mathbf{M})$ and the kinematic parameters $(\varepsilon_o, \boldsymbol{\chi})$.

In general, the solution of equations (1), (2)-(5) and (7) is not straightforward. In fact, the elastic modulus E depends on the martensite fraction ξ through relation (2), while the martensite fraction ξ is function of the stress, through the evolutionary equations (4)-(5). Furthermore, the stress depends on the position of the typical point in the cross-section of the beam through equation (1). Hence, the problem is nonlinear.

Analytical solutions are possible only in few simplified cases, as discussed in Appendix A. In general, the $(\varepsilon_o, \boldsymbol{\chi})$-$(N, \mathbf{M})$ relationships should be computed numerically and two numerical schemes are proposed in the following.

Let equations (7) be written in the equivalent form:

$$\begin{aligned} R_N &= N - \int_A \sigma \, dA = 0 \\ \mathbf{R}_M &= \mathbf{M} + \int_A \mathbf{p}\sigma \, dA = \mathbf{0} \end{aligned} \tag{8}$$

where R_N and $\mathbf{R}_M$ are residuals. In the following these equations are solved using a Newton algorithm [23]:

$$\begin{aligned} \left\{ \begin{array}{c} 0 \\ \mathbf{0} \end{array} \right\} &= \left\{ \begin{array}{c} R_N(\varepsilon_o^{k+1}, \boldsymbol{\chi}^{k+1}) \\ \mathbf{R}_M(\varepsilon_o^{k+1}, \boldsymbol{\chi}^{k+1}) \end{array} \right\} \\ &= \left\{ \begin{array}{c} R_N(\varepsilon_o^{k}, \boldsymbol{\chi}^{k}) \\ \mathbf{R}_M(\varepsilon_o^{k}, \boldsymbol{\chi}^{k}) \end{array} \right\} + \left[\begin{array}{cc} \dfrac{\partial R_N}{\partial \varepsilon_o} & \dfrac{\partial R_N}{\partial \boldsymbol{\chi}} \\ \dfrac{\partial \mathbf{R}_M}{\partial \varepsilon_o} & \dfrac{\partial \mathbf{R}_M}{\partial \boldsymbol{\chi}} \end{array} \right]_{(\varepsilon_o, \boldsymbol{\chi}) = (\varepsilon_o^k, \boldsymbol{\chi}^k)} \left\{ \begin{array}{c} \varepsilon_o^{k+1} - \varepsilon_o^k \\ \boldsymbol{\chi}^{k+1} - \boldsymbol{\chi}^k \end{array} \right\} \end{aligned} \tag{9}$$

where the superscripts ^{k} and $^{k+1}$ indicate the iteration indices. Given the k-th solution, i.e. $(\varepsilon_o^{[k]}, \boldsymbol{\chi}^{[k]})$, equation (9) can be solved in terms of $(\varepsilon_o^{[k+1]}, \boldsymbol{\chi}^{[k+1]})$. The derivative of the residuals are:

$$\begin{aligned} \frac{\partial R_N}{\partial \varepsilon_o} &= -\int_A \frac{\partial \sigma}{\partial \varepsilon_o} dA = -A_o \\ \frac{\partial R_N}{\partial \boldsymbol{\chi}} &= -\int_A \frac{\partial \sigma}{\partial \boldsymbol{\chi}} dA = -\mathbf{A}_1 \\ \frac{\partial \mathbf{R}_M}{\partial \varepsilon_o} &= \int_A \mathbf{p} \frac{\partial \sigma}{\partial \varepsilon_o} dA = -\mathbf{A}_2 \\ \frac{\partial \mathbf{R}_M}{\partial \boldsymbol{\chi}} &= \int_A \mathbf{p} \otimes \frac{\partial \sigma}{\partial \boldsymbol{\chi}} dA = -\mathbf{A}_3 \end{aligned} \tag{10}$$

where $\otimes$ denotes the dyadic product, A_o is a scalar, $\mathbf{A}_1$ and $\mathbf{A}_2$ are vectors and $\mathbf{A}_3$ is a matrix.

The computation of R_N and $\mathbf{R}_M$ and of their derivatives requires:

- the time integration of the local constitutive equations;
- the determination of the algorithmically tangent moduli $\partial\sigma/\partial\varepsilon_o$ and $\partial\sigma/\partial\boldsymbol{\chi}$;
- the evaluation of the integrals over the cross-section A.

The time integration of equations (4) and (5) in the interval $[t_n, t_{n+1}]$ is performed by a backward-Euler scheme:

$$\lambda = -(1-\xi) \frac{|\sigma| - |\sigma_n|}{|\sigma| - \sigma_f^{AS(\pm)}} \tag{11}$$

$$\lambda = \xi \frac{|\sigma| - |\sigma_n|}{|\sigma| - \sigma_f^{SA(\pm)}} \tag{12}$$

where :

$$\lambda = \int_{t_n}^{t_{n+1}} \dot{\xi} dt = \xi - \xi_n \tag{13}$$

To simplify the notation the subscript $_n$ indicates a quantity evaluated at time t_n while no subscript indicates a quantity evaluated at time t_{n+1}. The time discrete model is solved using a return map algorithm described in Reference [21].

The determination of the algorithmically tangent moduli $\partial\sigma/\partial\varepsilon_o$ and $\partial\sigma/\partial\boldsymbol{\chi}$ clearly depends on how the local time-discrete constitutive equations (2), (3), (11) and (12) are enforced. In the following two different approaches are discussed.

3.1 Scheme 1

In the first numerical scheme the local time-discrete constitutive equations (2), (3), (11) and (12) are continuously enforced in the whole cross-section of the beam. Their linearization gives, respectively:

$$\begin{aligned} dE &= E^\star d\xi \\ d\sigma &= E^{\star\star} d\xi + E d\varepsilon \\ 0 &= \alpha^{AS} d\xi + \beta^{AS} d\varepsilon \\ 0 &= \alpha^{SA} d\xi + \beta^{SA} d\varepsilon \end{aligned} \tag{14}$$

with:

$$\begin{aligned} E^\star &= E_A \left(\frac{E_A}{E_S} - 1\right) \left[1 + \left(\frac{E_A}{E_S} - 1\right) \xi\right]^{-2} \\ E^{\star\star} &= E^\star (\varepsilon - \xi\varepsilon_L) - E\varepsilon_L \\ \alpha^{AS} &= \text{sign}(\varepsilon)(1-\xi_n)E^{\star\star} + |\sigma_n| - \sigma_f^{AS} \\ \beta^{AS} &= \text{sign}(\varepsilon)(1-\xi_n)E \end{aligned} \tag{15}$$

do while (residuals $\leq$ tolerance)	
initialize quantities	
loop on the elements in the cross section	
loop on the Gauss points	
compute strain ε	[Eqn. (1.4)]
compute martensite fraction ξ	[Eqns. (11)-(12)]
compute stress σ	[Eqn. (3)]
add contribution to N and $\mathbf{M}$	
compute algorithmic tangent moduli	[Eqns. (16)-(17)]
add contribution to global tangent	[Eqn. (18)]
end loop	
end loop	
solve system	[Eqn. (9)]
compute new solution ε_o, $\boldsymbol{\chi}$	
compute new residuals	[Eqn. (8)]
end do	

Table 1: Scheme 1. Iteration procedure for each time step

$$\alpha^{SA} = -\operatorname{sign}(\varepsilon)\xi_n E^{\star\star} + |\sigma_n| - \sigma_f^{AS}$$
$$\beta^{SA} = -\operatorname{sign}(\varepsilon)\xi_n E$$

where sign($\bullet$) is the sign function. Hence, through equation (14), the tangent moduli are computed as:

$$\frac{\partial \sigma}{\partial \varepsilon_o} = \frac{\partial \sigma}{\partial \varepsilon}\frac{\partial \varepsilon}{\partial \varepsilon_o} = E_T \qquad \frac{\partial \sigma}{\partial \boldsymbol{\chi}} = \frac{\partial \sigma}{\partial \varepsilon}\frac{\partial \varepsilon}{\partial \boldsymbol{\chi}} = -\mathbf{p}E_T \tag{16}$$

where the consistent material tangent modulus $E_T = \partial\sigma/\partial\varepsilon$ is:

$$E_T = E + HE^{\star\star} \tag{17}$$

with $H = -\beta^{AS}/\alpha^{AS}$ for the conversion of austenite into martensite and $H = -\beta^{SA}/\alpha^{SA}$ for the conversion of martensite into austenite.

The substitution of equation (16) into (10) returns the explicit form for the quantities A_o, $\mathbf{A}_1$, $\mathbf{A}_2$ and $\mathbf{A}_3$:

$$A_o = \int_A E_T dA \qquad \mathbf{A}_1 = \mathbf{A}_2 = -\int_A \mathbf{p}E_T dA \qquad \mathbf{A}_3 = \int_A \mathbf{p}\otimes\mathbf{p}E_T dA \tag{18}$$

Finally, the integration over the cross-section to determine the residuals R_N and $\mathbf{R}_M$ and their derivatives A_o, $\mathbf{A}_1$, $\mathbf{A}_2$ and $\mathbf{A}_3$ is performed by discretizing the cross-section in quadrilateral finite-elements and applying Gauss integration formulas within each element.

The algorithmic implementation of the iterative procedure relative to Scheme 1 is briefly reported in Table 1.

3.2 Scheme 2

In the second numerical scheme a discretization of the martensite fraction ξ over the cross-section is introduced:

$$\xi = \sum_{i=1}^{n} \xi_i \phi_i \tag{19}$$

where $\phi_i = \phi_i(x, y)$ are interpolation functions, ξ_i are discrete parameters and n is the total number of discrete parameters in the cross–section. In particular, the cross-section is discretized in quadrilateral finite-elements; accordingly, the ϕ_i's are the usual piecewise bi-linear interpolation functions and the ξ_i's are the nodal martensite-fraction values.

Equations (2) and (3) are enforced in the whole section, as in the previous scheme. On the other hand, to determine the evolution of the ξ_i's, it is sufficient to enforce equations (11) and (12) only at the nodal points and not in the whole cross-section as done in the previous scheme.

In a similar way, to compute $\partial\sigma/\partial\varepsilon_o$ and $\partial\sigma/\partial\boldsymbol{\chi}$, the linearization of equations (11) and (12) is required only at the nodal points:

$$\begin{aligned} 0 &= \alpha_i^{AS} d\xi_i + \beta_i^{AS} d\varepsilon_i \\ 0 &= \alpha_i^{SA} d\xi_i + \beta_i^{SA} d\varepsilon_i \end{aligned} \tag{20}$$

where the subscript $_i$ denotes quantities evaluated at the $i-$th node. Taking into account expression (19), the linearization of the martensite fraction is:

$$d\xi = \sum_{i=1}^{n} d\xi_i \phi_i = \sum_{i=1}^{n} H_i \phi_i d\varepsilon_i = \sum_{i=1}^{n} H_i \phi_i \left(d\varepsilon_o - \mathbf{p}_i \bullet \boldsymbol{\chi} \right) \tag{21}$$

with $H_i = -\beta_i^{AS}/\alpha_i^{AS}$ or $H_i = -\beta_i^{SA}/\alpha_i^{SA}$. The substitution of $d\xi$ into the linearization of equations (2) and (3) allows the evaluation of the algorithmically consistent tangent moduli:

$$\begin{aligned} \frac{\partial \sigma}{\partial \varepsilon_o} &= E + E^{\star\star} \sum_{i=1}^{n} H_i \phi_i \\ \frac{\partial \sigma}{\partial \boldsymbol{\chi}} &= -\mathbf{p} E - E^{\star\star} \sum_{i=1}^{n} H_i \phi_i \mathbf{p}_i \end{aligned} \tag{22}$$

The quantities A_o, $\mathbf{A}_1$, $\mathbf{A}_2$ and $\mathbf{A}_3$ now specialize as follows:

$$\begin{aligned} A_o &= \int_A \left(E + E^{\star\star} \sum_{i=1}^{n} H_i \phi_i \right) dA \\ \mathbf{A}_1 &= -\int_A \left(\mathbf{p} E + E^{\star\star} \sum_{i=1}^{n} H_i \phi_i \mathbf{p}_i \right) dA \end{aligned} \tag{23}$$

do while (residuals $\leq$ tolerance)	
loop on the nodes in the cross section	
compute strain ε_i	[Eqn. (1.4)]
compute martensite fraction ξ_i	[Eqns. (11)-(12)]
end loop	
initialize quantities	
loop on the elements in the cross section	
loop on the Gauss points	
compute strain ε	[Eqn. (1.4)]
compute martensite fraction ξ	[Eqn. (19)]
compute stress σ	[Eqn. (3)]
add contribution to N and $\mathbf{M}$	
compute algorithmic tangent moduli	[Eqns. (22)-(17)]
add contribution to global tangent	[Eqn. (23)]
end loop	
end loop	
solve system	[Eqn. (9)]
compute new solution ε_o, $\boldsymbol{\chi}$	
compute new residuals	[Eqn. (8)]
end do	

Table 2: Scheme 2. Iteration procedure for each time step

$$\mathbf{A}_2 = -\int_A \mathbf{p}\left(E + E^{\star\star}\sum_{i=1}^{n} H_i\phi_i\right) dA$$

$$\mathbf{A}_3 = \int_A \mathbf{p}\otimes\left(\mathbf{p}E + E^{\star\star}\sum_{i=1}^{n} H_i\phi_i\mathbf{p}_i\right) dA$$

Due to the fact that for the present scheme $\mathbf{A}_1$ and $\mathbf{A}_2$ differ, equation (9) is now governed by an unsymmetric matrix.

The integration over the cross-section to determine the residuals R_N and $\mathbf{R}_M$ and their derivatives A_o, $\mathbf{A}_1$, $\mathbf{A}_2$ and $\mathbf{A}_3$ is performed by applying Gauss integration formulas within each finite-element of the cross-section.

The algorithmic implementation of the iterative procedure relative to Scheme 2 is briefly reported in Table 2. Accordingly, the nodal values of martensitic fraction are initially updated over the whole cross-section. Then, the resultants are computed through the integration of the stress evaluated with formulas (19) and (3).

It can be emphasized that in Scheme 1 the martensite fraction is computed at each Gauss point solving the corresponding evolutionary equation, in Scheme 2 the martensite fraction is computed at each Gauss point through the interpolation formula, properly updated enforcing the evolutionary equations only at the nodes.

4 SMA finite element

The finite element formulation is performed introducing an approximation on the displacement field $(w, \mathbf{s})$. The axial displacement w is taken to be linear along the beam axis, while the transverse displacement v is interpolated by the classical Hermite shape functions as required by the Euler-Bernoulli beam theory:

$$w = \mathbf{B}_w \widehat{\mathbf{w}} = \left[\begin{array}{cc} \frac{(1-\eta)}{2} & \frac{(1+\eta)}{2} \end{array} \right] \left[\begin{array}{c} \widehat{w}_1 \\ \widehat{w}_2 \end{array} \right] \tag{24}$$

$$\mathbf{s} = \mathbf{B}_s \widehat{\mathbf{s}} = \left[\begin{array}{cccccccc} B_s^1 & 0 & B_s^2 & 0 & B_s^3 & 0 & B_s^4 & 0 \\ 0 & B_s^1 & 0 & B_s^2 & 0 & B_s^3 & 0 & B_s^4 \end{array} \right] \left[\begin{array}{c} \widehat{u}_1 \\ \widehat{v}_1 \\ \widehat{\theta}_1^x \\ \widehat{\theta}_1^y \\ \widehat{u}_2 \\ \widehat{v}_2 \\ \widehat{\theta}_2^x \\ \widehat{\theta}_2^y \end{array} \right]$$

where $\eta = 2\zeta/L$, with $\zeta \in [-L/2, L/2]$, $\widehat{\theta}_i^j$ is the rotation about the $j-$axis at the $i-$node, $\widehat{u}_i, \widehat{v}_i, \widehat{w}_i$ are the displacement of the $i-$node, and

$$\begin{aligned} B_s^1 &= \frac{(\eta+2)(\eta-1)^2}{4} \\ B_s^2 &= \frac{L(\eta+1)(\eta-1)^2}{8} \\ B_s^3 &= \frac{(\eta-2)(\eta+1)^2}{4} \\ B_s^4 &= \frac{L(\eta-1)(\eta+1)^2}{8} \end{aligned} \tag{25}$$

Substitution of the interpolation functions in the principle of virtual work gives the equilibrium equations for the FE beam:

$$L_{vi} = \int_L \left(\mathbf{M} \bullet \mathbf{B}_s^{''} \delta\widehat{\mathbf{s}} + N \mathbf{B}_w^{'} \delta\widehat{\mathbf{w}} \right) d\zeta \tag{26}$$

Using formulas (7), the linearization of equation (26) leads to the form of the tangent stiffness matrix $\mathbf{K}_T$, to be used in the solution of nonlinear FE problems through a Newton technique:

$$\mathbf{K}_T = \left[\begin{array}{cc} \mathbf{K}_T^{ww} & \mathbf{K}_T^{ws} \\ \mathbf{K}_T^{sw} & \mathbf{K}_T^{ss} \end{array} \right] \tag{27}$$

where

$$\mathbf{K}_T^{ww} = \int_L \left[\left(\mathbf{B}_w^{'} \right)^t A_o \mathbf{B}_w^{'} \right] d\zeta \tag{28}$$

$$
\begin{aligned}
\mathbf{K}_T^{ws} &= \int_L \left[\left(\mathbf{B}_w^{''} \right)^t \mathbf{A}_1 \mathbf{B}_s^{'} \right] d\zeta \\
\mathbf{K}_T^{sw} &= \int_L \left[\left(\mathbf{B}_s^{''} \right)^t \mathbf{A}_2 \mathbf{B}_w^{'} \right] d\zeta \\
\mathbf{K}_T^{ss} &= \int_L \left[\left(\mathbf{B}_s^{''} \right)^t \mathbf{A}_3 \mathbf{B}_s^{''} \right] d\zeta
\end{aligned}
$$

The integration along the ζ-coordinate is performed numerically by Gauss formulas. It can be noted that the element stiffness is symmetric only when $\mathbf{A}_1 = \mathbf{A}_2$, which occurs using Scheme 1 for the cross-section solution. This aspect may make Scheme 1 computationally more advantageous than Scheme 2.

5 Numerical Applications

In the following a set of examples are considered to investigate the overall ability of the proposed procedures to study SMA structures. Initially, the attention is concentrated on the response of a single cross-section, i.e. the axial force and the bending moment are taken constant along the beam axis. Then, more general examples, e.g. four- and three-point bending tests, are considered, for which experimental data are available in literature.

Two Ni-Ti shape-memory alloys are considered. The first material, produced by GAC International Inc., is a commercial superelastic Ni-Ti orthodontic straight wire with rectangular cross-section of dimensions $h = 0.64$ mm and $b = 0.46$ mm. Based on the experimental data presented in [24] and relative to a tensile test performed at temperature $T = 50^o$C, the material parameters in traction are set equal to the values indicated in Table 3.

E_A	$= 47000$ MPa	,	E_S	$= 17000$ MPa	, $\varepsilon_L^+ = 10\%$
$\sigma_s^{AS,+}$	$= 350$ MPa	,	$\sigma_f^{AS,+}$	$= 350$ MPa	
$\sigma_s^{SA,+}$	$= 125$ MPa	,	$\sigma_f^{SA,+}$	$= 125$ MPa	

Table 3: GAC shape-memory alloy: material parameter in traction

The second material, produced by Nitinol Device & Components, Inc. (NDC), is a commercial superelastic Ni-Ti straight wire with circular cross-section of diameter $D = 1.49$ mm. Based on the experimental data presented in [19] and relative to tensile tests, the material parameters in traction are set equal to the values indicated in Table 4.

E_A	$= 60000$ MPa	,	E_S	$= 20000$ MPa	, $\varepsilon_L^+ = 7.5\%$
$\sigma_s^{AS,+}$	$= 520$ MPa		$\sigma_f^{AS,+}$	$= 600$ MPa	
$\sigma_s^{SA,+}$	$= 300$ MPa		$\sigma_f^{SA,+}$	$= 200$ MPa	

Table 4: NDC shape-memory alloy: material parameter in traction

It can be noted that the phase transformations occur at constant stress values in the first material, while the starting and the final stress differ in the second material.

In the following, only the case of simple bending is considered, i.e. $M_y = 0$ and $M_x = M$. Hence, due to the symmetry of the cross-sections considered, $\chi_y = 0$ and $\chi_x = \chi$.

Finally, the numerical integration along the length of the beam is performed using six Gauss integration points per element. For the evaluation of the cross-section integrals, 20 strips orthogonal to the y-axis are used for Scheme 1; similarly, 21 discrete parameters are used for the cross-section interpolation of the martensite fraction ξ for Scheme 2, corresponding again to 20 strips orthogonal to the y-axis. For both schemes, 4 Gauss points of integration are employed in each strip. Accordingly, at the cross-section level Scheme 2 is computationally less expensive than Scheme 1.

5.1 Cross-section response

To focus on the cross-section response, a beam subjected only to a bending moment constant along the axis is studied; hence, $N = 0$.

Initially, to test the accuracy of the proposed algorithmic solution schemes, a comparison between analytical and numerical solutions is performed for the case of a loading-unloading cycle in terms of bending moment. Recalling that analytical solutions are possible only under restrictive hypotheses (see Appendix A), equal material properties in traction and compression and equal austenite and martensite elastic moduli ($E_A = E_S = 47000$ MPa) are assumed. The GAC Ni-Ti alloy is considered.

In Figure 2 the bending moment versus the curvature is plotted; the excellent match between the numerical and analytical solutions shows the overall performance of the proposed numerical procedures.

However, as previously emphasized, experimental evidence shows not only a difference between the martensite and the austenite elastic properties, but also a difference between the material response in traction and in compression. Hence, $E_A \neq E_S$ as given in Table 3, while the material properties in compression are indicated in Table 5.

$\sigma_s^{SA,-} = 700$ MPa	,	$\sigma_f^{AS,-} = 700$ MPa	,	$\varepsilon_L^- = 7\%$
$\sigma_s^{SA,-} = 250$ MPa	,	$\sigma_f^{SA,-} = 250$ MPa	,	

Table 5: GAC shape-memory alloy: material parameter in compressiom

Again, a loading-unloading cycle in terms of bending moment is performed. In Figures 3 and 4 the curvature χ and the axial strain ε_o are plotted versus the bending moment M for the two numerical schemes considered.

It can be observed that the two solutions show almost no difference in terms of bending moment versus curvature, while they present some differences in terms of bending moment versus axial strain. In particular, the solution relative to Scheme 2 is less smooth than the one relative to Scheme 1. This difference in

smoothness is related to the fact that in Scheme 2 the martensite evolutionary equation is enforced only at the nodes, while in Scheme 1 it is enforced at each Gauss point. Hence, due to the specific choice of number of elements in the cross-section versus the number of Gauss points per element, at the cross-section level Scheme 2 is computationally less expensive than Scheme 1, but at the same time it is also less accurate. According to these considerations, the forthcoming simulations are performed using only Scheme 1.

In particular, Figure 4 shows that the axial strain has a non monotonic response with respect to the moment, even during the loading path. This effect can be well interpreted looking at the stress distribution over the cross-section for different loading levels. In Figures 5 and 6 the stress distribution are plotted for M = 20,25,40 N*mm and for M = 40,15,7.5 N*mm, respectively, while the corresponding curvatures and axial strains are evidenced with stars in Figures 3 and 4.

During the loading process the stress distribution in the cross-section evolves as discussed in the following.

1. At the beginning no phase transformation occurs in the cross-section. Thus, the material response is linearly elastic and the neutral axis remains at zero.
2. Since the value of the stress transformation is higher in compression than in tension, the phase transformation starts first on the part of the cross-section in traction, then also on the part in compression ($M = 20$ N*mm). Moreover, to get a zero axial resultant, the neutral axis starts to move downward (Figure 5) and an axial deformation shows up (Figure 4).
3. As soon as the phase transformation is completed on the part of the cross-section in traction, a material restiffening in that area is encountered. Hence, a progressive upward movement of the neutral axis occurs, together with a reduction of the axial deformation. In particular, a stress reduction can be observed in part of the cross-section, even leading to the activation of the reverse phase transformation from martensite to austenite (this explains the presence of a flat stress distribution for y approximately between -0.05 and 0).

During the unloading process the stress pattern become more and more complex because of the combination of the neutral axis movement and the different material response in tension and in compression.

5.2 Three point bending

The case of a simply supported beam subjected to a pointwise central force is considered. The beam has length $L = 14$ mm, and it is made of GAC wire. Due

to symmetry conditions, only half of the beam is considered. A mesh of 10 beam elements is used for the analysis.

The comparison between the numerical solution and the experimental results is presented in terms of the applied force versus the midspan inflection. In Figure 7 the material is assumed to have equal response in tension and compression, as given in Table 3. In Figure 8 different material response in tension and compression is considered, as given in Tables 3 and 5. While the first simulation (Figure 7) underestimates the experimentally observed beam behavior, the second one (Figure 8) show a good match at least for the loading path. The difference between the numerical and experimental results, observed in Figure 8 during the initial portion of the unloading, can be attributed to frictional effects of the supports not taken into account in the present analysis.

5.3 Four point bending

A simply supported beam subjected to two pointwise equal forces F is considered. The beam has length $L = 20$ mm, and the distance between the two applied forces is $L_F = L/3$. The beam is made of NDC circular wire.

The comparison between the numerical solution and the experimental results is presented in terms of the applied force F versus the midspan inflection in Figure 9. A good match between the numerical and the experimental curves is found, in particular for the loading path.

Finally, a comparison of the results obtained using the proposed beam model and the full three-dimensional elasticity model presented in [19] is given in Figure 10. The simulations show the good performance of the simple beam model.

6 Conclusions

The present work addresses a simple and effective tool for the analysis of superelastic 1D structural elements.

The structural model is developed following the classical Euler-Bernoulli beam theory, which requires the use of a 1D constitutive relationship. In particular, the SMA constitutive model adopted herein takes into account the different material response in tension and compression as well as the different elastic properties between austenite and martensite.

Two numerical procedures are developed for the determination of the cross-section response. The implementation of the SMA beam model in a finite-element framework is also addressed.

Several numerical examples are investigated. Due to the peculiar material behavior, the cross-section shows an unusual response also for the very simple case of pure bending. In particular, a non-monotonic relation between the applied moment and the axial strain is highlighted.

Using the proposed finite-element beam formulation, four- and three-point bending tests are studied. The numerical results show a good agreement with available experimental data and, in particular, with the numerical results obtained from a three-dimensional finite-element analysis.

Accordingly, it is possible to conclude that the presented formulation represents a valid and effective computational tool for the analysis of SMA 1D structural elements.

Acknowledgments

The authors would like to thank professor F. Maceri for many interesting and useful discussions as well as professor Airoldi and professor Riva for making available to the authors the experimental data relative to the three-point bending test.

The financial supports of the Italian National Research Council (CNR), of the Ministry of University and Research (MURST) and of the Italian Space Agency (ASI) are gratefully acknowledged.

References

[1] C.M. Wayman and T.W. Duerig. An introduction to martensite and shape memory. In T.W. Duerig, K.N. Melton, D. Stökel, and C.M. Wayman, editors, *Engineering aspects of shape memory alloys*, pages 3–20, 1990.

[2] C.M. Wayman. Shape memory and related phenomena. *Progress in Material science*, 36:203–224, 1992.

[3] C.M. Wayman. Shape memory alloys. *MRS bulletin*, April:49–56, 1993.

[4] A.G. Khachaturyan. *Theory of structural transformations in solids.* John Wiley & Sons, 1983.

[5] C.M. Wayman. *Introduction to the crystallography of martensitic transformations.* MacMillan, 1964.

[6] H. Funakubo. *Shape memory alloys.* Gordon and Breach Science Publishers, 1987. translated from the Japanese by J.B. Kennedy.

[7] T.W. Duerig, K.N. Melton, D. Stökel, and C.M. Wayman, editors. *Engineering aspects of shape memory alloys.* Butterworth-Heinemann, 1990.

[8] A.R. Pelton, D. Hodgson, and T. Duerig, editors. *Proceedings of the First International Conference on Shape Memory and Superelastic Technologies*, 1994.

[9] R.C.L. Sachdeva and S. Miyazaki. Superelastic Ni-Ti alloys in orthodontics. In T.W. Duerig, K.N. Melton, D. Stökel, and C.M. Wayman, editors, *Engineering aspects of shape memory alloys*, pages 452–469, 1990.

[10] A. Melzer and D. Stökel. Performance improvement of surgical instrumentation through the use of Ni-Ti materials. In A.R. Pelton, D. Hodgson, and T. Duerig, editors, *Proceedings of the First International Conference on Shape Memory and Superelastic Technologies*, pages 401–409, 1994.

[11] L.C. Brinson and R. Lammering. Finite-element analysis of the behavior of shape memory alloys and their applications. *International Journal of Solids and Structures*, 30:3261–3280, 1993.

[12] F. Trochu and Yuan-Yao Qian. Nonlinear finite element simulation of superelastic shape memory alloy parts. *Computers & Structures*, 62:799–810, 1997.

[13] J. Lubliner and F. Auricchio. Generalized plasticity and shape memory alloys. *International Journal Solids and Structures*, 33:991–1003, 1996.

[14] P.H. Adler, W. Yu, A.R. Pelton, R. Zadno, T.W. Duerig, and R. Barresi. On the tensile and torsional properties of pseudoelastic Ni-Ti. *Scripta Metallurgica et Materialia*, 24:943–947, 1990.

[15] K.N. Melton. Ni-Ti based shape memory alloys. In T.W. Duerig, K.N. Melton, D. Stökel, and C.M. Wayman, editors, *Engineering aspects of shape memory alloys*, pages 21–35, 1990.

[16] T. Atanackovic and M. Achenbach. Moment-curvature relations for a pseudoelastic beam. *Continuum Mechanics and Thermodynamics*, 1:73–80, 1989.

[17] Y. Gillet, E. Patoor, and M. Berveiller. Elements of structure calculation for shape memory devise. *Journal de Physique IV, Colloque C4*, 1:151–156, 1991.

[18] Y. Gillet, E. Patoor, and M. Berveiller. Beam theory applied to shape memory alloy. In *Proceedings of the First International Conference on Shape Memory and Superelastic Technologies*, pages 169–174, 1994.

[19] F. Auricchio. *Shape-memory alloys: Applications, micromechanics, macromodelling and numerical simulations*. PhD dissertation, University of California at Berkeley, Department of Civil Engineering, 1995.

[20] F. Auricchio, R.L. Taylor, and J. Lubliner. Shape-memory alloys: macromodelling and numerical simulations of the superelastic behavior. *Computer Methods in Applied Mechanics and Engineering*, 1997. Accepted for publication.

[21] F. Auricchio and E. Sacco. A one-dimensional model for superelastic shape-memory alloys with elastic properties between austenite and martensite. *International Journal of Non-Linear Mechanics*, 1997. Accepted for publication.

[22] E.P. Popov. *Engineering Mechanics of Soilds*. Prentice-Hall, 1990.

[23] D.G. Luenberger. *Introduction to Linear and Nonlinear Programming*. Addison-Wesley Publishing Company, 1973.

[24] G. Airoldi, G. Riva, and M. Vanelli. Superelasticity and shape-memory effect in Ni-Ti orthodontic wires. In *Proceedings of the International Conference on Martensitic Transformations (ICOMAT)*, 1995.

Appendix A. An analytical solution

As discussed in Section 3, the relation between the stress resultants $(N, \mathbf{M})$ and the kinematic parameters $(\varepsilon_o, \boldsymbol{\chi})$ are nonlinear. However, an analytical expression for the $(\varepsilon_o, \boldsymbol{\chi})$-$(N, \mathbf{M})$ relation can be obtained under the following simplifying assumptions:

- equal material response in tension and compression,
- equal elastic properties between austenite and martensite ($E_A = E_S = E$),
- equal initial and final values for the phase transformations ($\sigma_s^{AS} = \sigma_f^{AS} = \sigma^{AS}$ and $\sigma_s^{SA} = \sigma_f^{SA} = \sigma^{SA}$),
- pure bending loading state ($N = M_y = 0$, $M_x = M$).

The discussion is herein restricted to the case of a rectangular cross-section with dimensions b and h; the extension to other cross-section geometries can be easily performed.

As a direct consequence of the pure bending state and of the symmetry of the cross-section, $\varepsilon_o = \chi_y = 0$ and $\chi_x = \chi$. During the loading ($\dot{M} > 0$), three different stress distributions along the cross-section are possible. The three stress distributions correspond to three different load levels and are schematically reported in Figure 11. The quantities y_1 and y_2 are defined as:

$$y_1 : \qquad E\ \varepsilon(y_1) = \sigma^{AS} \qquad \text{with} \quad 0 \le y_1 \le \frac{h}{2}$$

$$y_2 : \qquad E\left[\varepsilon(y_2) - \varepsilon_L\right] = \sigma^{AS} \qquad \text{with} \quad 0 \le y_2 \le \frac{h}{2}$$

Accordingly, y_1 and y_2 can be computed as:

$$\begin{aligned} y_1 &= \max\left[\min\left(\frac{\sigma^{AS}}{E\chi}, \frac{h}{2}\right), 0\right] \\ y_2 &= \max\left[\min\left(\frac{\sigma^{AS} + E\varepsilon_L}{E\chi}, \frac{h}{2}\right), 0\right] \end{aligned}$$

Performing the integration of the stresses over the cross-section, the moment-curvature relationship is obtained:

$$\frac{M}{b} = \frac{E}{3}\left[\frac{h^3}{4} + \frac{2}{3}\left({y_1}^3 - {y_2}^3\right)\right]\chi + E\varepsilon_L\left({y_2}^2 - \frac{h^2}{4}\right) + \sigma^{AS}\left({y_2}^2 - {y_1}^2\right) \qquad (29)$$

During the unloading ($\dot{M} < 0$), three other stress distributions along the cross-section are possible. Again, the stress distributions correspond to different load

levels and are schematically reported in Figure 11. The quantities η_1, η_2 and η_3 are defined as:

$$\eta_1 : \quad E\left[\varepsilon(\eta_1) - \varepsilon_p(\eta_1)\right] = \sigma^{SA} - \sigma^{AS} \quad \text{with} \quad y_{1,p} \leq \eta_1 \leq y_{2,p}$$

$$\eta_2 : \quad E\left[\varepsilon(\eta_2) - \varepsilon_L\right] = \sigma^{SA} \quad \text{with} \quad y_{2,p} \leq \eta_2 \leq \frac{h}{2}$$

$$\eta_3 : \quad E\ \varepsilon(\eta_3) = \sigma^{SA} \quad \text{with} \quad y_{1,p} \leq \eta_3 \leq \frac{h}{2}$$

where the subscript $_p$ indicates quantities evaluated at the end of the loading process. Accordingly, η_1, η_2 and η_3 can be computed as:

$$\begin{aligned}
\eta_1 &= \max\left[\min\left(\frac{\sigma^{SA} - \sigma^{AS}}{E(\chi - \chi_p)}, y_{2,p}\right), y_{1,p}\right] \\
\eta_2 &= \max\left[\min\left(\frac{-\sigma^{SA} + E\varepsilon_L}{E\chi}, \frac{h}{2}\right), y_{2,p}\right] \\
\eta_3 &= \max\left[\min\left(\frac{\sigma^{SA}}{E\chi}, \frac{h}{2}\right), y_{1,p}\right]
\end{aligned}$$

Performing the integration of the stresses over the cross-section, the moment-curvature relationship is obtained:

$$\begin{aligned}
\frac{M}{b} &= \frac{E}{3}\left[\frac{h^3}{4} + \frac{2}{3}\left({\eta_3}^3 + {\eta_1}^3 - {\eta_2}^3 - y_{1,p}^3\right)\right]\chi + \\
&\quad E\left[\varepsilon_L\left({\eta_2}^2 - \frac{h^2}{4}\right) + \frac{2}{3}\chi_p\left(y_{2,p}^2 - y_{1,p}^2\right)\right] + \\
&\quad \sigma^{AS}\left({\eta_1}^2 - y_{1,p}^2\right) + \sigma^{SA}\left({\eta_2}^2 - {\eta_4}^2\right)
\end{aligned} \tag{30}$$

where $\eta_4 = \max(\eta_1, \eta_2)$.

The presented formulas are different in form but equivalent to those proposed in Reference [16]. It is important to observe that the necessary simplifications introduced to obtain a closed-form solution may be too simplified to properly reproduce the real SMA material behavior.

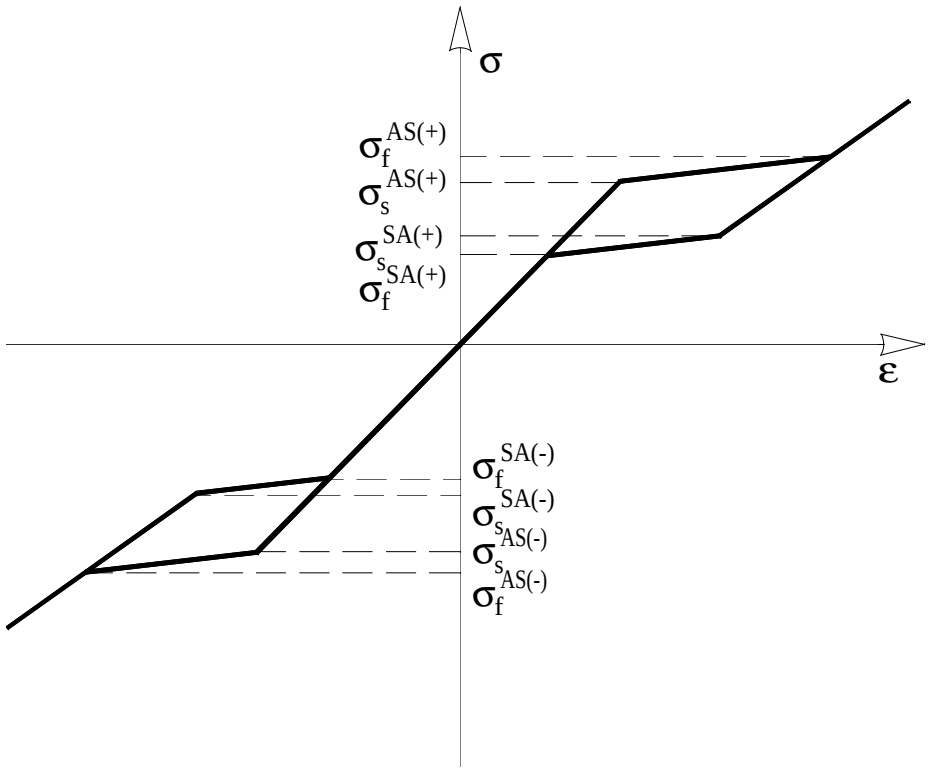

Figure 1: One-dimensional superelastic behavior of a shape-memory alloy. Experimental evidences show different material properties between traction and compression as well as different elastic properties between austenite and martensite.

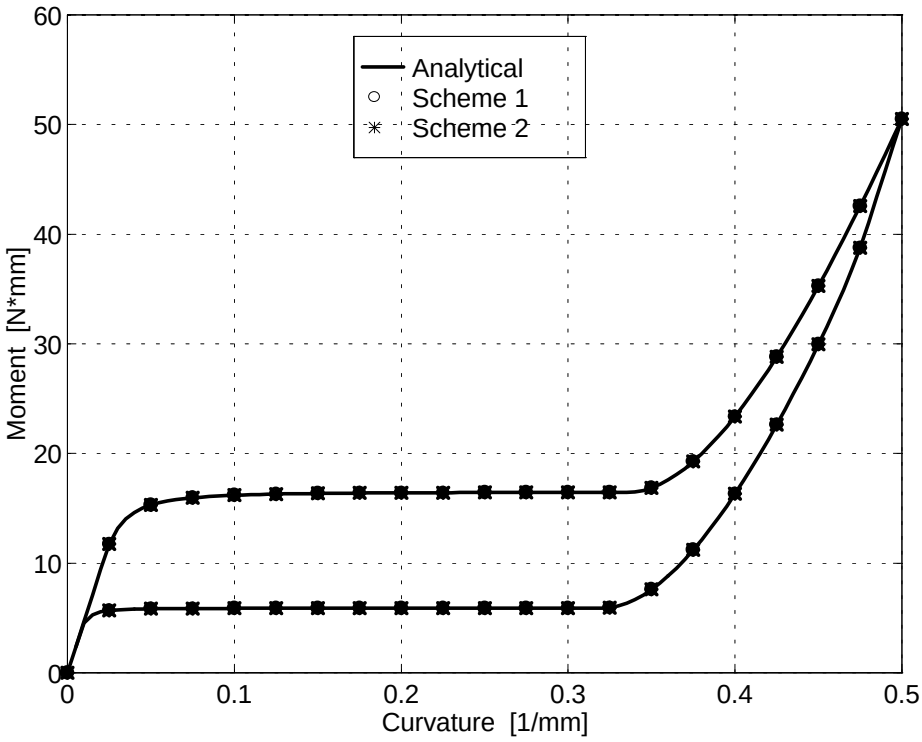

Figure 2: Pure bending for a section of GAC Ni-Ti alloy with equal properties in traction and compression and equal elastic moduli between austenite and martensite. Moment vs curvature. Comparison between the analytical and numerical solutions.

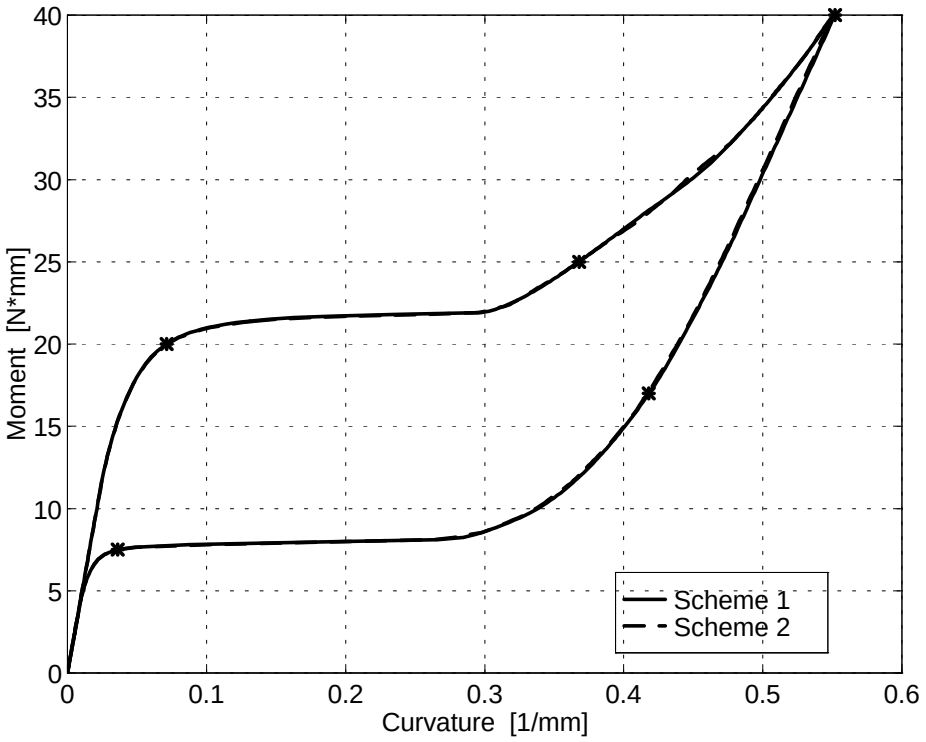

Figure 3: Pure bending for a section of GAC Ni-Ti alloy with different properties in traction and compression and different elastic moduli between austenite and martensite. Moment vs curvature. Numerical solution.

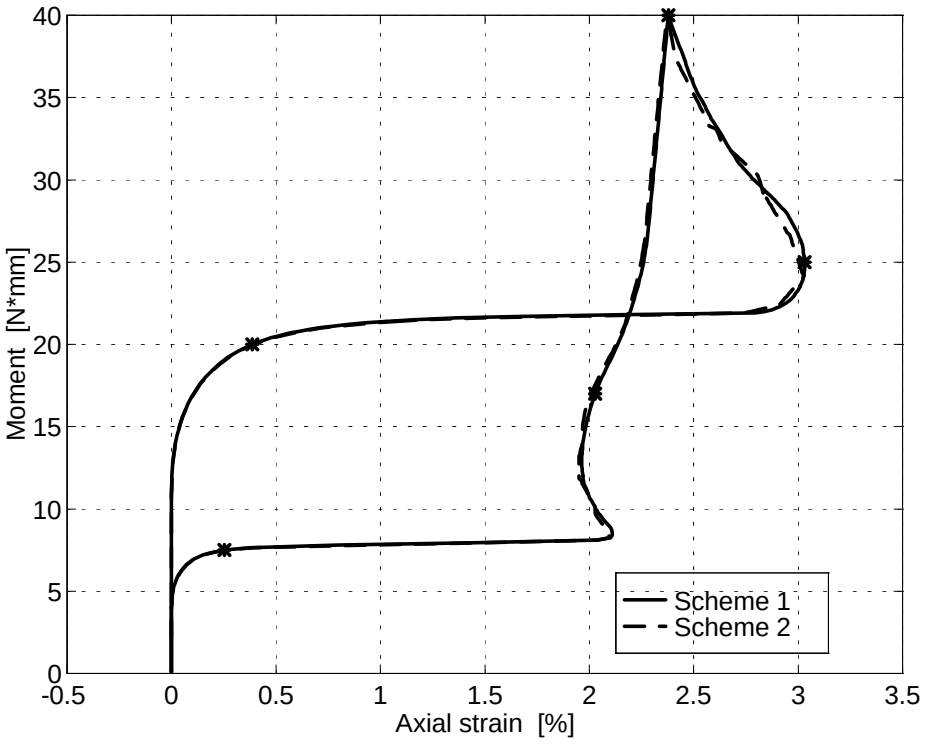

Figure 4: Pure bending for a section of GAC Ni-Ti alloy with different properties in traction and compression and different elastic modulus between austenite and martensite. Moment vs axial strain. Numerical solution.

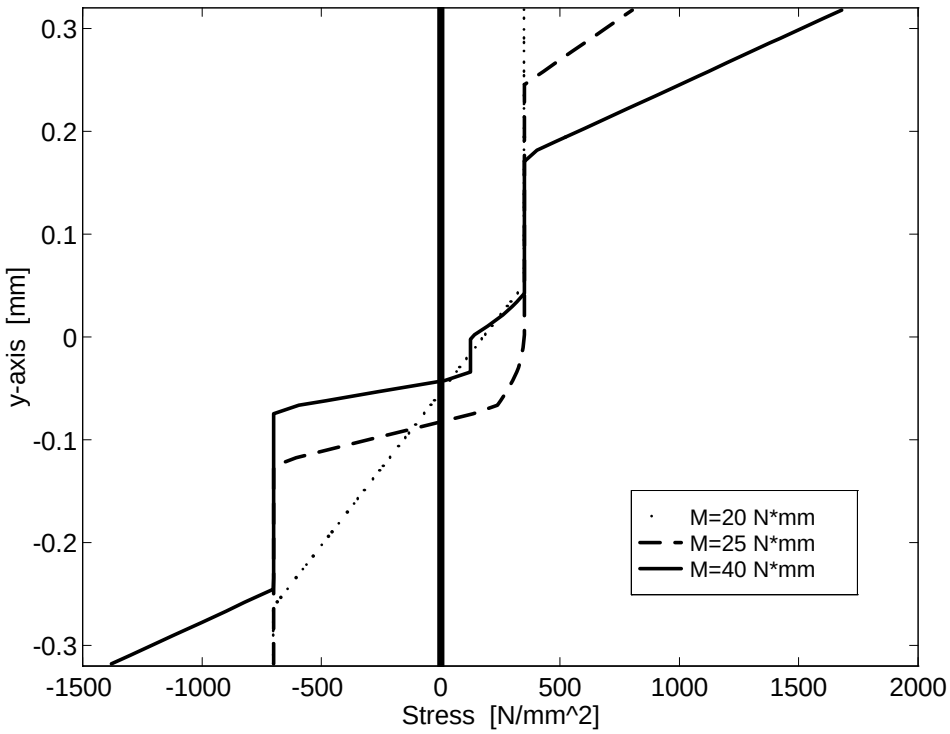

Figure 5: Pure bending for a section of GAC Ni-Ti alloy with different properties in traction and compression and different elastic moduli for austenite and martensite. Stress distribution along the cross-section at different load levels. Loading path.

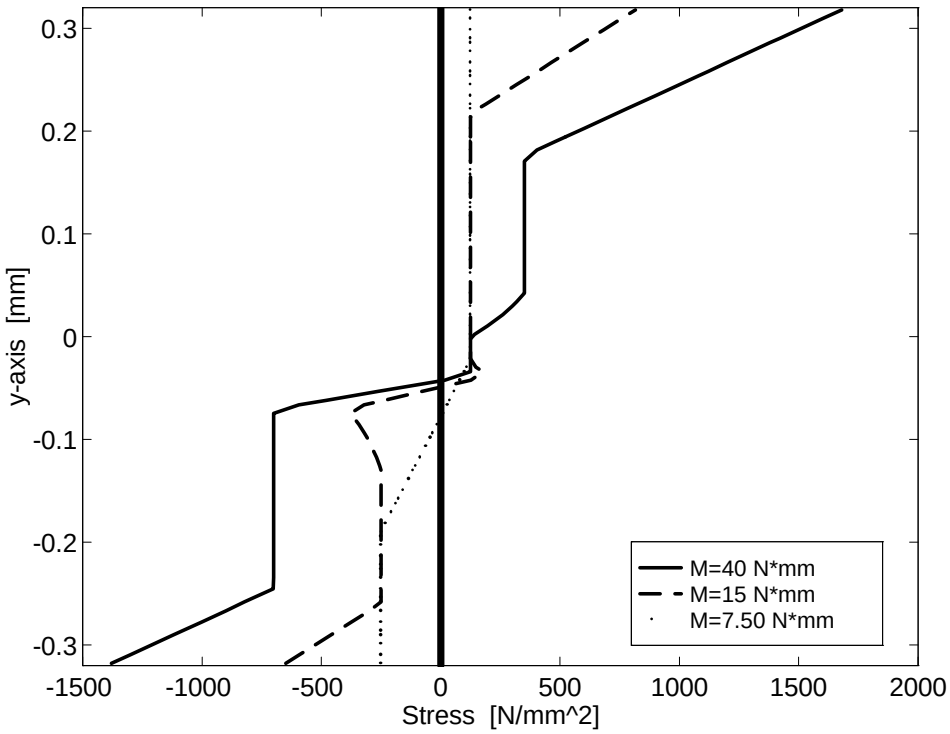

Figure 6: Pure bending for a section of GAC Ni-Ti alloy with different properties in traction and compression and different elastic moduli between austenite and martensite. Stress distribution along the cross-section at different load levels. Unloading path.

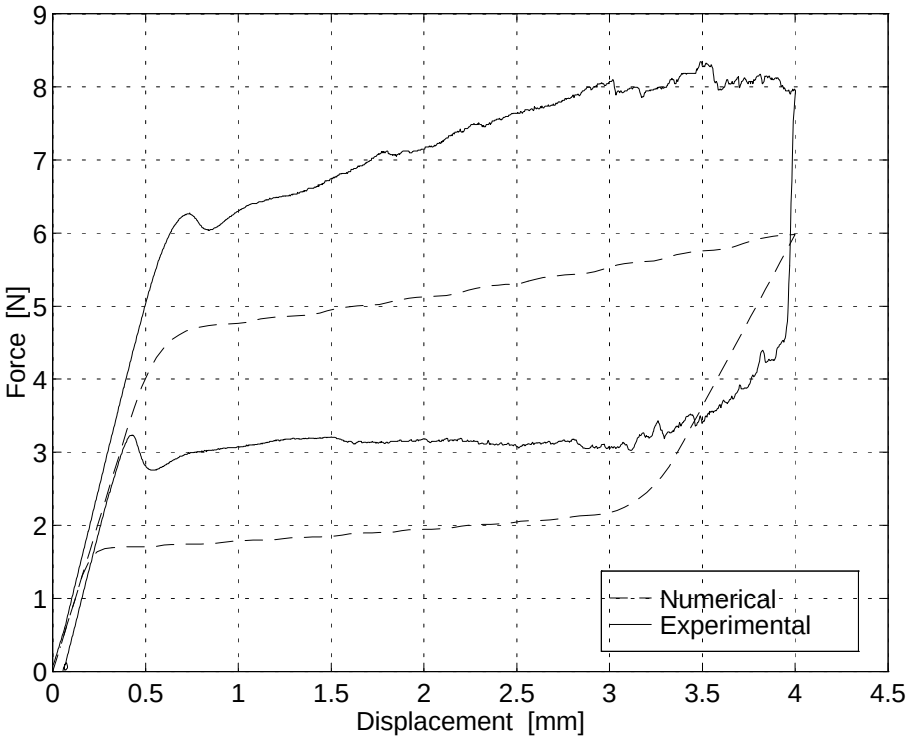

Figure 7: Three-point bending test for a GAC wire with equal properties in traction and in compression and different elastic moduli between austenite and martensite: applied force F versus midspan inflection. Comparison between numerical and experimental results.

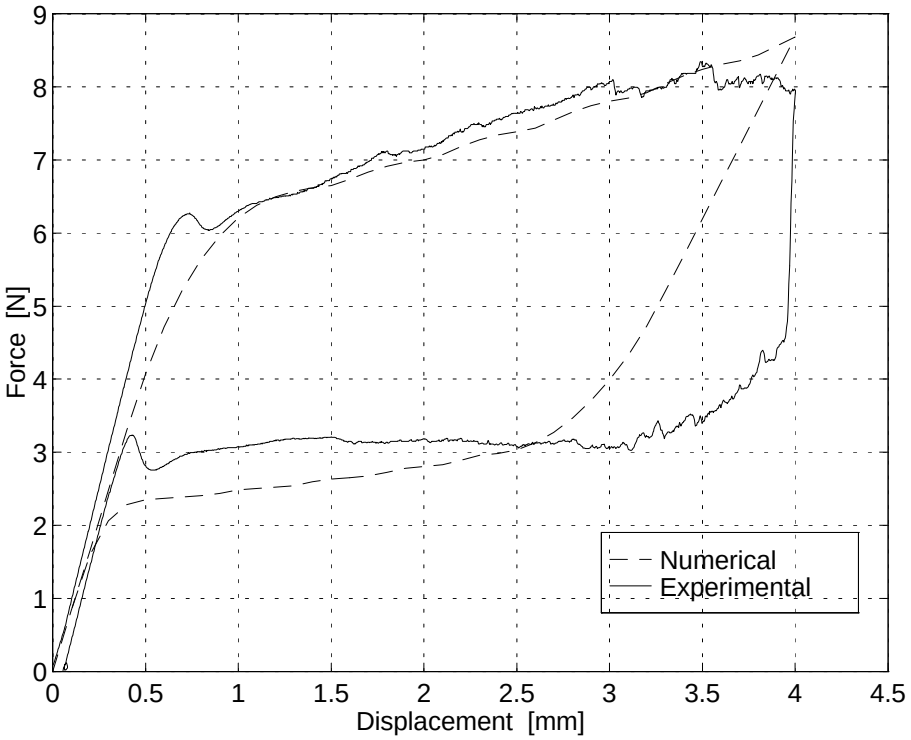

Figure 8: Three-point bending test for a GAC wire with different properties in traction and in compression and different elastic moduli between austenite and martensite: applied force F versus midspan inflection. Comparison between numerical and experimental results.

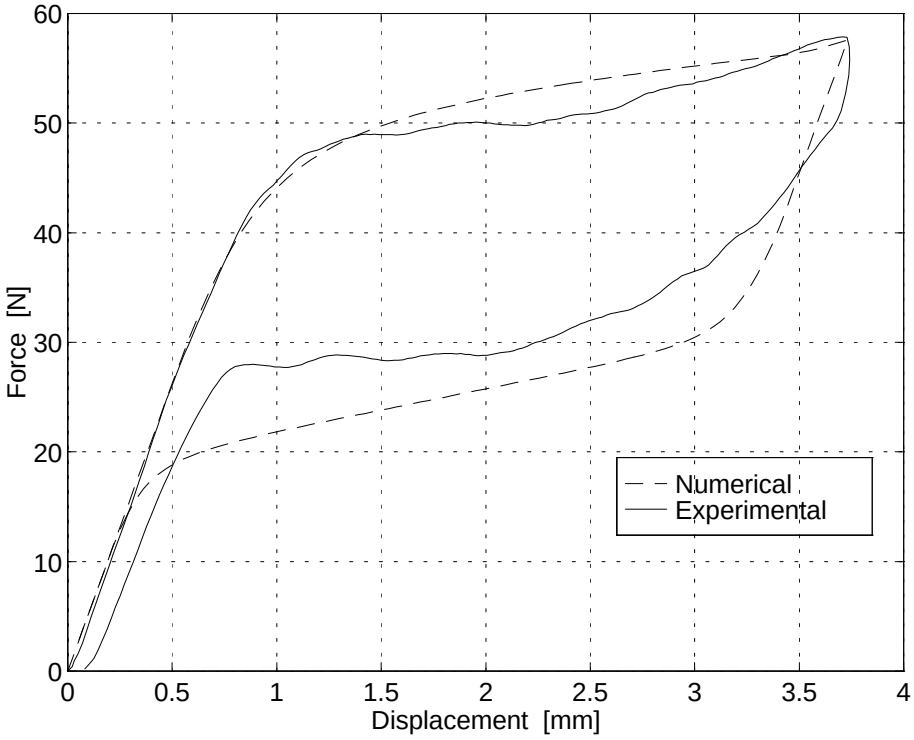

Figure 9: Four-point bending test for a NDC wire with different properties in traction and in compression and equal elastic moduli between austenite and martensite: applied force F versus midspan inflection. Comparison between numerical and experimental results.

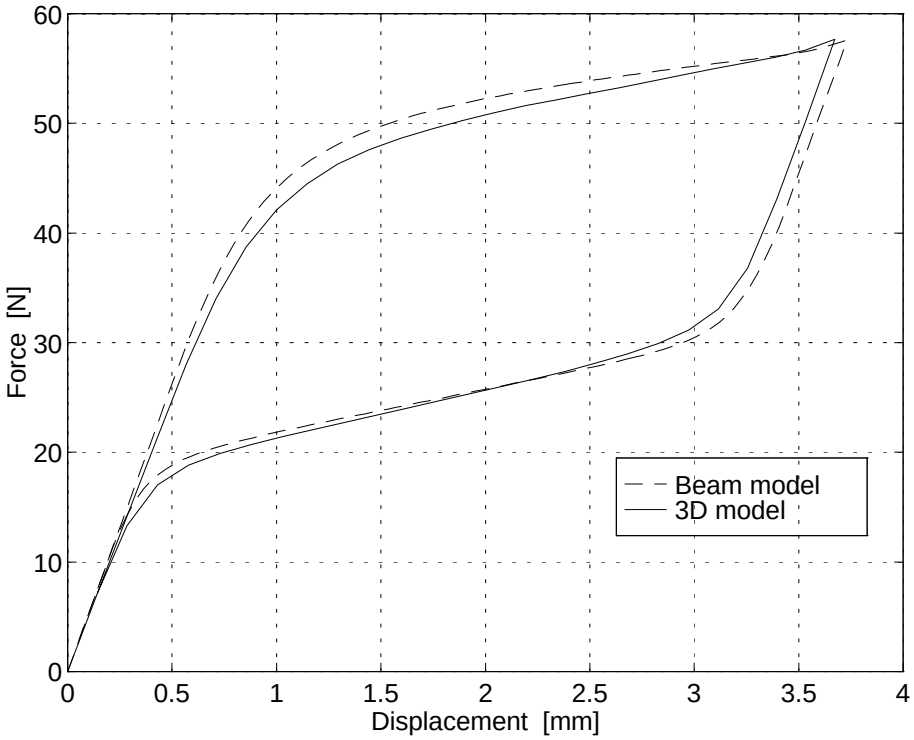

Figure 10: Four-point bending test for a NDC wire with different properties in traction and in compression and equal elastic moduli between austenite and martensite: applied force F versus midspan inflection. Comparison between beam and three-dimensional analyses.

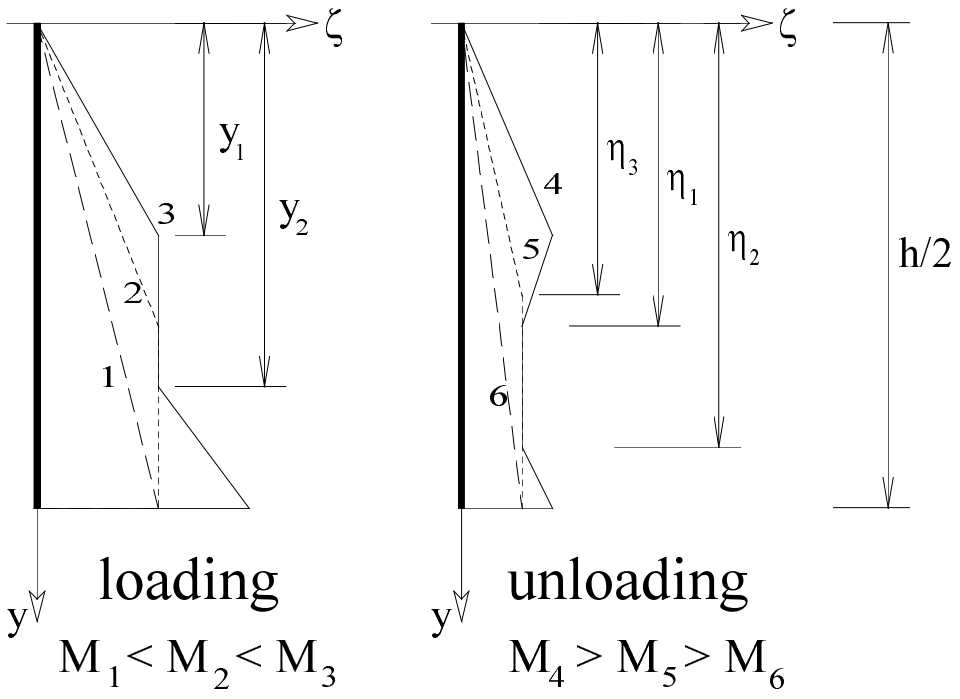

Figure 11: Pure bending: analitical solution. Possible stress distributions in the cross-section during the loading and the unloading.